

Article

Effect of Carrier Gas Flow Rate on the Morphology and Luminescence Properties of CsPbBr₃ Microcrystals

Xiaoting Wang, Fangfang You, Jianping Huang, Yi Yao and Faqiang Xu * 

National Synchrotron Radiation Laboratory, School of Nuclear Science and Technology, University of Science and Technology of China, Hefei 230029, China; sa1923@mail.ustc.edu.cn (X.W.); youff@mail.ustc.edu.cn (F.Y.); hjp613@mail.ustc.edu.cn (J.H.); yiyao@mail.ustc.edu.cn (Y.Y.)

* Correspondence: fqxu@ustc.edu.cn

Abstract: All-inorganic halide perovskites, especially lead perovskite microcrystals, have attracted more and more attention because of their excellent photoelectric properties and chemical stability. Herein, high quality CsPbBr₃ microcrystals with three different stable morphologies, namely microplate, frustum of a square pyramid and pyramid, were synthesized by the chemical vapor deposition (CVD) method through altering the flow rate of a carrier gas and were comparatively studied in structure and optical property. The photoluminescence (PL) results showed that the CsPbBr₃ microplate has the best luminescence property. The structural characterization results by scanning electron microscope (SEM), X-ray photoelectron spectroscopy (XPS), X-ray diffraction (XRD), X-ray rocking curves (XRC) and Raman revealed that the flow rate of the carrier gas could manipulate the morphology evolution of CsPbBr₃ microcrystals and further impact their luminescence properties.

Keywords: all-inorganic lead halide perovskite; CsPbBr₃; structure–function relationship; morphology; crystal growth; luminescence



Citation: Wang, X.; You, F.; Huang, J.; Yao, Y.; Xu, F. Effect of Carrier Gas Flow Rate on the Morphology and Luminescence Properties of CsPbBr₃ Microcrystals. *Crystals* **2022**, *12*, 479. <https://doi.org/10.3390/cryst12040479>

Academic Editors: Aldo Di Carlo, Emmanuel Kymakis, Mahmoud Zendeheel, Narges Yaghoobi Nia, Mohsen Ameri, Seyedal Emami and Shujun Zhang

Received: 6 March 2022

Accepted: 27 March 2022

Published: 31 March 2022

Publisher's Note: MDPI stays neutral with regard to jurisdictional claims in published maps and institutional affiliations.



Copyright: © 2022 by the authors. Licensee MDPI, Basel, Switzerland. This article is an open access article distributed under the terms and conditions of the Creative Commons Attribution (CC BY) license (<https://creativecommons.org/licenses/by/4.0/>).

1. Introduction

Lead halide perovskite (LHP) APbX₃ (A = CH₃NH₃⁺, CH(NH₂)₂⁺, Cs⁺, X = Cl[−], Br[−], and I[−]) materials have gained substantial attention over the past decades [1–7], owing to their excellent characteristics, including broadly tunable band gaps, high photoluminescence (PL) quantum efficiency, low nonradiative recombination rate, and direct band-gap [8–11]. For this reason, a large number of LHP-based photoelectric devices have been developed, including solar cells, low-threshold lasers, bright light-emitting diodes (LEDs) and photodetectors [12–15].

Among the various types of LHP-based devices, the ones based on organic–inorganic hybrid perovskites usually exhibit excellent performance because of the mutual modulation effects between organic and inorganic components. However, the issue of stability is a crucial factor for realizing the expected potential of such kind of solar cells [16]. Organic–inorganic hybrid perovskites are found to decompose easily in a humid environment on account of the existence of hygroscopic amine salt [17,18], and they show low thermal stability even in an inert atmosphere [19]. Comparatively, all-inorganic halide perovskite, which was first reported by Møller in 1958 [20], possesses a stronger tolerance for moisture, oxygen, heat, light, and electrical field. For example, Jin et al. reported an all-inorganic solar capacitor by integrating a perovskite solar cell unit and a supercapacitor unit into a single device that exhibits high open-circuit voltage and outstanding stability [21]. Xue et al. developed a self-powered, high-performance CsPbBr₃ perovskite photodetector that shows the responsivity and detectivity of 0.3 A/W and 1.15 × 10¹³ cm·Hz^{1/2}/W, respectively, and has an anti-corrosion ability to water and alcohol [22]. Apart from outstanding stability, all-inorganic perovskites can also have a high light-harvesting capability [23] and display strong PL emission with narrow full width at half maximum (FWHM), with a PL quantum yield up to ~90% [24]. Besides, all-inorganic perovskites can also be doped

by other elements and show more excellent properties. For example, Mn-doped CsPbCl₃ nanocrystals (NCs) with high Mn substitution synthesized at room temperature showed excellent stability and luminescence property [25]. In addition, all-inorganic perovskites can be fabricated in heterojunction with other semiconductor materials to obtain more outstanding optoelectronic performance. For example, P.K. Giri et al. fabricated a vertical heterojunction photodetector with integrating CsPbBr₃ nanocrystals on a large-area monolayer MoS₂, and the photodetector showed a high responsivity (24.3 A W⁻¹ at 405 nm) and extremely fast photo response with photocurrent growth and decay times of 5.5 and 24.0 μs, respectively [26]. Therefore, all-inorganic perovskites have been intensively investigated from the synthesis of crystals to optoelectronic properties. Compared with organic–inorganic hybrids perovskites, all-inorganic perovskites have many different morphologies, which are highly conducive for studying the principle of intrinsic properties. However, the electrical and optical properties of all-inorganic perovskites with different morphologies still have not been studied widely [27,28].

At present, wet chemistry, a common synthesis method, is widely used to synthesize all-inorganic perovskites. Although people could get high quality perovskites by using wet chemistry, it may introduce unnecessary impurities from solvents and surfactants. In contrast, all-inorganic perovskite crystals that were synthesized by chemical vapor deposition (CVD) have higher purity [29] and have no ligands or other impurities, which are beneficial for us to study the intrinsic properties of perovskites. Recent studies have found that the process parameters of CVD, such as temperature, pressure, growth time, etc., can sometimes significantly influence the morphology and further impact the property of the samples. The effect of the flow rate of a carrier gas, one of the key parameters in the CVD process, is intensively explored in the growth of crystals such as graphene and MoS₂ [30,31]. However, there are still few reports about how the flow rate affects the growth of CsPbBr₃.

Here, CsPbBr₃ microcrystals with three different morphologies, namely microplate, frustum of a square pyramid and pyramid, were synthesized by adjusting the flow rate of the carrier gas in the CVD process. A scanning electron microscope (SEM) and atomic force microscope (AFM) were used to explore the morphology, while X-ray rocking curve (XRC), X-ray diffraction (XRD), X-ray photoelectron spectroscopy (XPS) and Raman were applied to investigate the structure of the CsPbBr₃ microcrystals. The PL results revealed the luminescence properties of CsPbBr₃ microcrystals. The diversity of morphologies of all-inorganic perovskite microcrystals were demonstrated, and the relationship between intrinsic structure and optical properties was explored. Our findings provided a new insight into the structure–function relationship of all-inorganic perovskites, which can be a valuable reference for design of outstanding photoelectric devices.

2. Materials and Methods

Materials: High-purity (>98%) PbBr₂ powder was bought from Alfa Aesar. CsBr powder with a purity of 99.5%, acetone and ethanol were purchased from Sinopharm Chemical Reagent Co., Ltd. The silicon wafer (diameter: 100 mm, thickness: 525 μm) obtained from HeFei Crystal Technical Material Co., Ltd. (Hefei, China) was cleaved into 50 × 20 mm slices, which were used as the substrate.

Pretreatment of substrate: The silicon substrate was first washed ultrasonically at room temperature in acetone, ethanol and deionized water for 15 min separately to remove the organic contaminants on the surface, was then placed into the piranha solution at 90 °C for 2 h to dissolve the oxide overlayer, and lastly, was cleaned and dried by deionized water and ultrahigh purity N₂.

Synthesis of CsPbBr₃ perovskite microcrystals: The CsPbBr₃ perovskite microcrystals were synthesized by a vapor-phase method using a home-built CVD system that was equipped with a tube furnace having two heating zones, as shown in Figure 1. The source materials were the mixed powder of PbBr₂ (36.7 mg) and CsBr (42.6 mg) with a molar ratio of 1:2, and then they were placed into a quartz boat. Next, the quartz boat was placed into

the center of heating zone I of the furnace. The silicon substrate was placed in the center of heating zone II with a distance of about 20 cm from the source materials. The quartz tube was first evacuated to a low vacuum state by a turbo molecular pump, and then it was filled with a high-purity Ar carrier gas with a flow rate of 40–120 sccm until the inner pressure reached 380 Torr. In the process of preparing the sample, zone I and zone II of the furnace were heated simultaneously to a temperature of 600 and 340 °C, respectively, which is the optimal condition to grow the target samples. The growth process lasted for 70 min at such a status and finished by stopping the heating of the furnace and allowing the system to cool down to room temperature naturally.

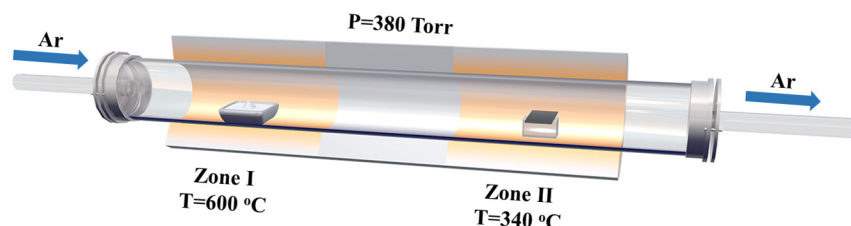


Figure 1. Schematic diagram of the CVD system.

Characterization: The morphologies and elemental mapping information of the CsPbBr₃ microcrystals were obtained using SEM (HITACHI, SU8220, Tokyo, Japan) and the accessory energy distribution spectroscopy (EDS) method. The AFM images of the CsPbBr₃ microcrystals were obtained using the Atomic Force Microscope (Veeco, diInnova, New York, NY, USA).

The XPS tests were performed to obtain the oxidation states of the elements in the CsPbBr₃ microcrystals. The XPS was conducted at room temperature using the spectrometer (Thermo Scientific Escalab 250, Westborough, MA, USA) equipped with an aluminum anode.

The phase and structure information of CsPbBr₃ microcrystals was collected at room temperature by using the Rigaku TTR-III X-ray diffractometer equipped with Cu K α radiation. The XRC were scanned using a high-resolution X-ray diffractometer (Malvern PANalytical, X'Pert3 MRD, Waltham, MA, USA) to investigate the quality of the CsPbBr₃ microcrystals.

Time-resolved photoluminescence results were collected from a Lecroy (New York, NY, USA) Wave Runner 6100 Digital Oscilloscope (1 GHz) equipped with a tunable laser (pulse width = 4 ns, gate = 500 ns) as the excitation source.

The Raman results were obtained on the HORIBA (Jobin Yvon, Paris, French) LabRAM HR Evolution system using a 633 nm laser light at room temperature.

For the purpose of detecting the optical property of the CsPbBr₃ microcrystals, the PL measurements were carried out at room temperature on the HORIBA LabRAM HR Evolution system by using an excitation laser with a wavelength of 325 nm at constant power mode.

The Raman and PL measurements were performed on a single microcrystal.

3. Results and Discussion

In the process of preparing CsPbBr₃ perovskite materials using the CVD method, we found three typical microcrystals with the morphologies of a microplate, frustum of a square pyramid and pyramid, which could be repeatedly synthesized simply by controlling the flow rate of the carrier gas Ar when the other growth parameters are optimized and fixed. Figure 2a–c showed the SEM images of the samples on the silicon substrate obtained at a flow rate 40, 80 and 120 sccm, respectively. As we can see, the microcrystals in the form of the microplate, frustum of a square pyramid and pyramid dominated in number in each corresponding image. However, the densities of the pyramid and frustum of a square pyramid were higher than that of microplate. This phenomenon is not hard to understand

since a higher flow rate of carrier gas leads to more nucleation, which would further evolve into higher crystallite density. The morphologies of the three kinds of microcrystals were verified by the AFM images and the scanned profile curves along the labeled lines in Figure 3a–c, respectively. All three microcrystals we selected have sharp edges: the square microplate in Figure 3a has a side length of about 10 μm and height of less than 1 μm , the frustum of a square pyramid in Figure 3b has an upper side length of about 7 μm , down side length of 10 μm and height of 2 μm , and the pyramid in Figure 3c has a width of about 8 μm and height of 4 μm . The AFM results indicate that the microplate tended to grow in two dimensions, while the frustum of a square pyramid and pyramid preferred to grow in three dimensions.

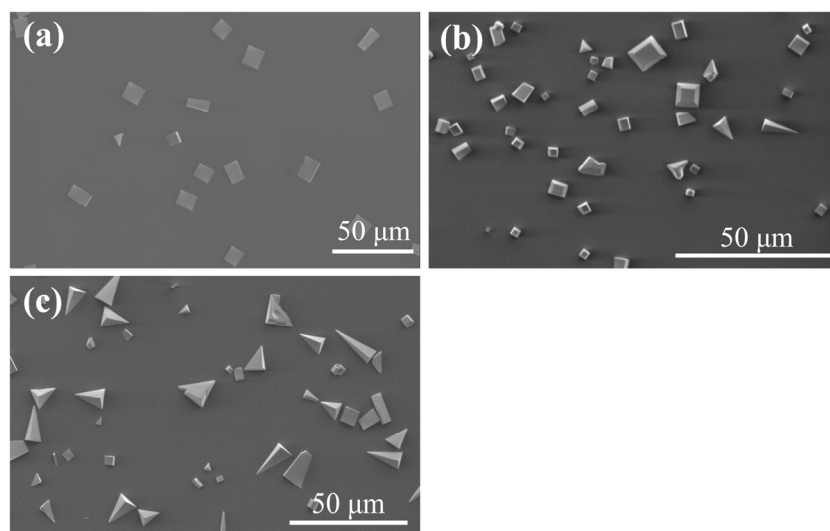


Figure 2. The SEM images of the microcrystals synthesized at the carrier gas flow rate of (a) 40, (b) 80, and (c) 120 sccm, respectively. Heating temperature of the source: 600 $^{\circ}\text{C}$. Substrate temperature: 340 $^{\circ}\text{C}$. Inner pressure: 380 Torr. Molar ratio of PbBr_2 and CsBr : 1:2.

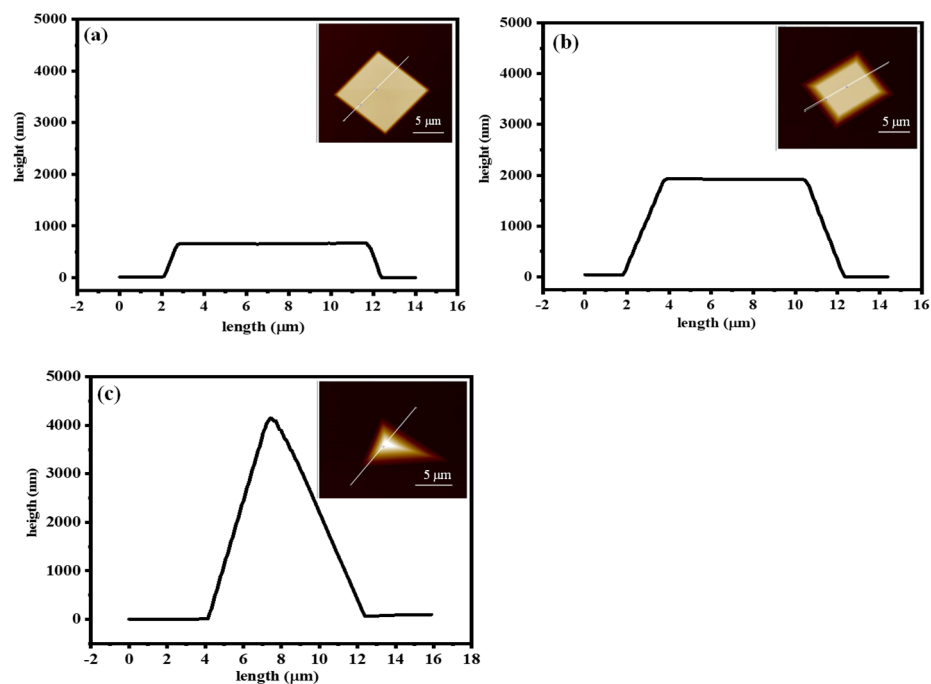


Figure 3. The AFM images and corresponding profile curves of the microplate (a), frustum of a square pyramid (b), and pyramid (c).

Then, the elemental composition and chemical stoichiometry of the microcrystals with different morphologies were analyzed by using energy dispersive spectroscopy (EDS), and the results are shown in Figure 4. As the elemental mappings in the illustration of Figure 4a–c demonstrate, all three kinds of microcrystals are composed of the elements Cs, Pb and Br, which are distributed uniformly and overlap perfectly in the microcrystals. Based on the weight percentages of the three elements shown in Figure 4, the atomic ratios of Cs: Pb: Br in the microplate, frustum of a square pyramid and pyramid are calculated to be 17.31:17.72:50.44, 17.16:17.76:50.56, and 16.17:17.19:53.69, respectively, which are all tightly close to the expected stoichiometric ratio of CsPbBr₃ (1:1:3). Thus, it was necessary to determine the oxidation states of the three elements in the microcrystals by the technique XPS. Figure 5a–c demonstrates, respectively, the high-resolution core level XPS spectra of Cs, Pb and Br for the three kinds of microcrystals. From Figure 5, all the spin-orbit split doublets of Cs 3d, Pb 4f and Br 3d levels can be clearly observed, and the binding energies and spectral shapes reveal that the three elements are in the valence states of Cs⁺, Pb²⁺ and Br[−], respectively, which are well consistent with the previous report [32]. There were small differences in the binding energies of Cs 3d, Pb 4f, and Br 3d among these microcrystals with different morphologies, which means that the bonding structure of them are almost the same; the differences may come from the defects and the instrumental errors.

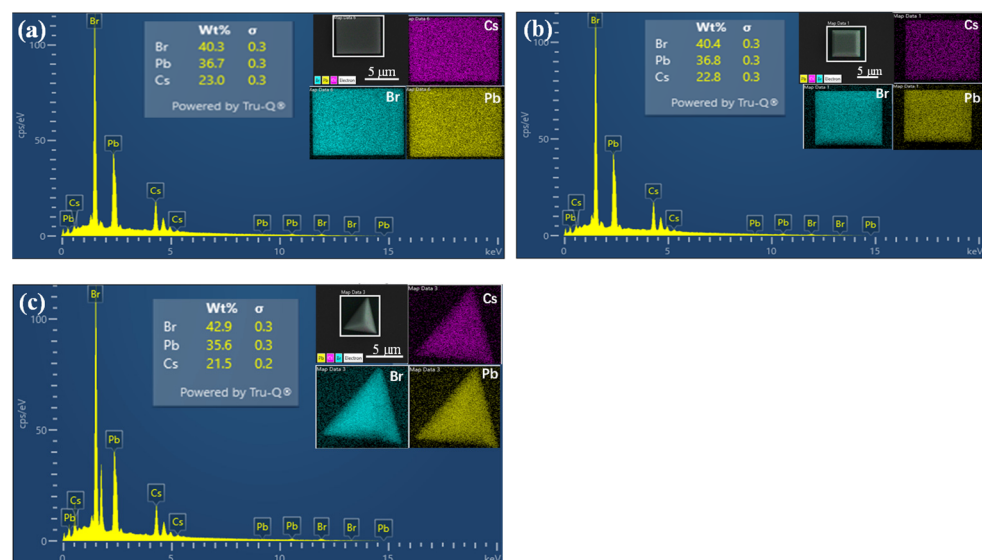


Figure 4. The EDS spectra and corresponding elemental mappings of the microplate (a), frustum of a square pyramid (b) and pyramid (c).

The above results indicate that the three kinds of microcrystals might be formed by the CsPbBr₃ perovskites. Therefore, the XRD technique was applied to detect the crystal structures and phase information of the three microcrystals. The XRD pattern of the sample containing microplate, as displayed in Figure 6a, shows three strong and sharp diffraction peaks at 15.4°, 30.6° and 30.9°, which were indexed respectively to the (100), (002), (200) facets of the CsPbBr₃ monoclinic phase [33]. While for the XRD spectra of the samples containing the frustum of a square pyramid and pyramid, besides the dominant peaks at 15.4°, 30.6° and 30.9°, two extra peaks at 21.7° and 44.2° became obvious, which can be indexed to the (-110) and (-220) facets of the monoclinic-phase CsPbBr₃, respectively. This behavior indicates that there emerged a new orientation during the growth of the CsPbBr₃ frustum of a square pyramid and pyramid. From the XRD patterns, we can conclude that the morphologies of the CsPbBr₃ microcrystals are closely related to the flow rate of the carrier gas. At a low flow rate, the microplate grew slowly and orderly in two dimensions along the c-axis of the (100) direction, with the (100) plane as the terminal surface of the microcrystal, while the proportions of the side face for the frustum of a square pyramid

and pyramid increased with the rise of the flow rate. This phenomenon may indicate that at a high flow rate, the mass transfer rate becomes faster, which means that the initial atoms may not have enough time to move into the right lattice location, where crystal domains can have the lowest surface free energy. Therefore, the subsequent atoms would grow in some specific direction in which the surface free energy of the crystal could decrease. As a consequence, CsPbBr₃ microcrystals displayed different morphologies by altering the flow rate of the carrier gas. A similar growth mechanism has also been proposed by Ting Yu et al. in MoS₂ crystal growth under different flow rates of carrier gas [34]. There were other little miscellaneous XRD peaks for the three CsPbBr₃ microcrystals, which indicated that they all have the same pure phases and good crystalline quality. Apart from XRD, Raman spectra were also measured to study the structure of the CsPbBr₃ microcrystals. The three spectra all showed well-resolved scattering bands at 73 cm⁻¹, 127 cm⁻¹ and 310 cm⁻¹ assigned to the vibrational modes of [PbBr₆]⁴⁻, the motion of Cs⁺ cations and the second-order phonon mode of octahedron, respectively, which exist typically in CsPbBr₃ perovskites [35,36].

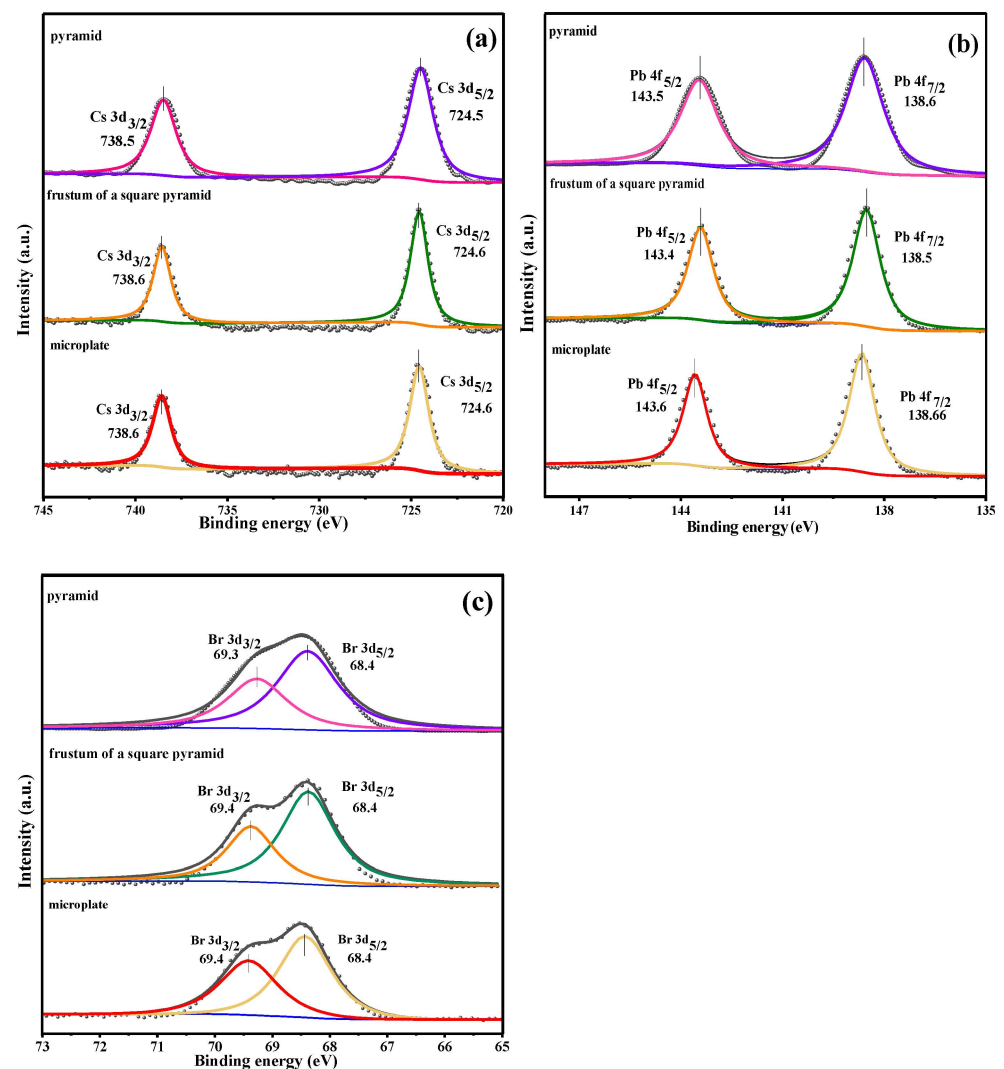


Figure 5. The XPS spectra of CsPbBr₃ microplate, frustum of a square pyramid, and pyramid for Cs 3d (a), Pb 4f (b), and Br 3d (c).

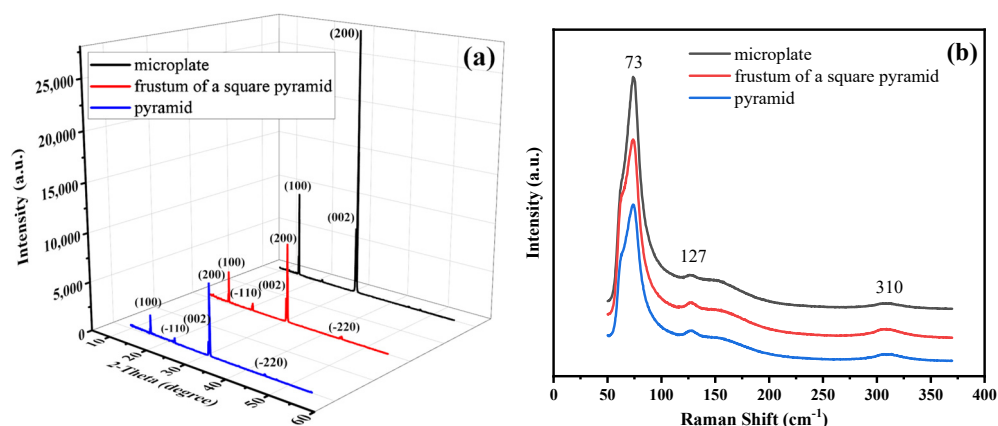


Figure 6. The XRD patterns (a) and Raman spectra (b) of the samples containing the microplate, frustum of a square pyramid, and pyramid. All the XRD peaks with 2θ above 10° can be well indexed to the monoclinic-phase CsPbBr_3 (JCPDS card 18-0364).

As a strong common method to determine the crystalline quality of the crystal [37], the XRC measurement was also carried out and the (200) facet's rocking curves of CsPbBr_3 microplate, frustum of a square pyramid and pyramid are shown in Figure 7. In general, a small FWHM represents good quality of crystal, low dislocation density and small residual stress in the crystal [38]. As Figure 7 shows, the FWHM of the CsPbBr_3 microplate, frustum of a square pyramid and pyramid is 0.32° , 0.53° , 0.51° , respectively. The FWHM of each curve is small and close to each other. These results indicate that all of the CsPbBr_3 microcrystals have good crystalline quality, which is consistent with the XRD result mentioned above.

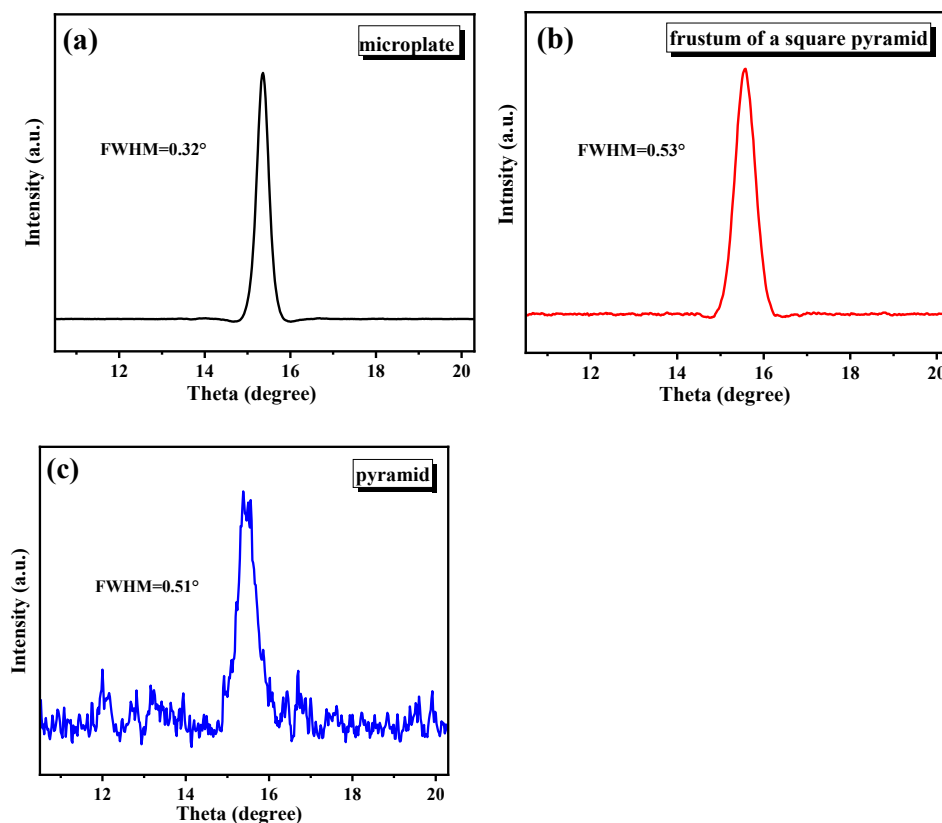


Figure 7. Rocking curve of the CsPbBr_3 microplate (a), frustum of a square pyramid, (b) and pyramid (c).

For the CsPbBr₃ microcrystals, their optical properties were of most concern; thus, PL measurements were performed to explore the optical characteristics of the three kinds of CsPbBr₃ microcrystals. As shown in Figure 8, the PL emissions of the CsPbBr₃ microplate, frustum of a square pyramid and pyramid are all located at around 2.3 eV, while the luminous intensities of them are obviously different. The PL intensity of the CsPbBr₃ microplate is the strongest, which is 1.4 times that of the frustum of a square pyramid and 2.2 times that of the pyramid. This result indicated that the flow rate of the carrier gas could manipulate the morphology evolution of CsPbBr₃ microcrystals and further impact their luminescence properties.

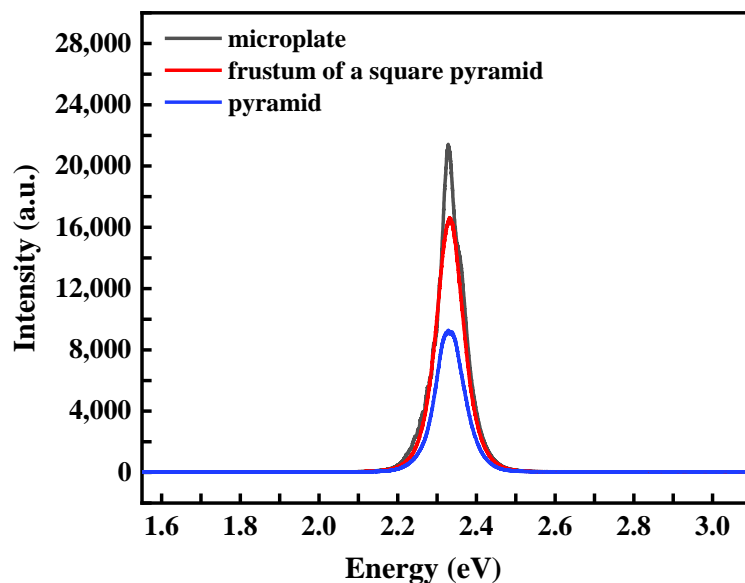


Figure 8. The PL spectra of the CsPbBr₃ microplate, frustum of a square pyramid, and pyramid.

For the CsPbBr₃ microplate with the strongest PL intensity, we further studied its long-term stability and time-resolved photoluminescence (TRPL). As shown in Figure 9a, the diffraction peaks of the microplate after 80 days of storage in ambient condition are still strong and sharp, which means that the microplate owns strong-phase stability. Figure 9b illustrates that the microplate has a good stability in optical properties, since the PL intensity of the microplate after 80 days of storage only has a small decrease compared with the fresh microplate. TRPL decay profiles of the microplate show that its average lifetime (τ_{ave}) is about 117 ns (Figure 9c).

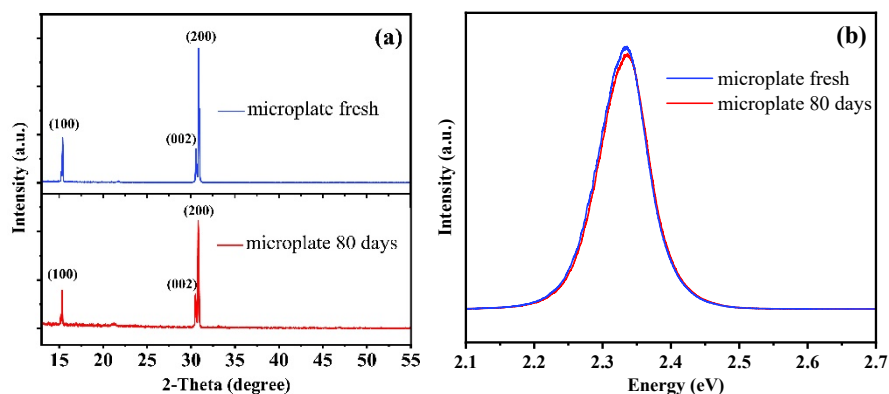


Figure 9. Cont.

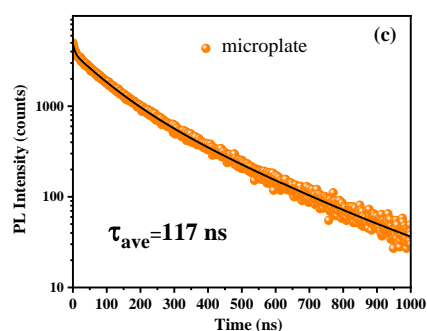


Figure 9. Comparison of the XRD pattern (a) and PL spectra (b) of a fresh CsPbBr₃ microplate and after 80 days of storage in ambient condition. (c) TRPL decay profile of the CsPbBr₃ microplate.

4. Conclusions

In summary, the microplate, frustum of a square pyramid and pyramid of CsPbBr₃ microcrystals were synthesized by regulating the flow rate of a carrier gas in the CVD process. The XRD results indicated that the three CsPbBr₃ microcrystals all have pretty good crystalline structure. The PL spectra showed that the CsPbBr₃ microplate displayed the best luminescence property among them. This result indicated that the flow rate of the carrier gas could manipulate the morphology evolution of the CsPbBr₃ microcrystals and further impact their luminescence properties. In addition, the CsPbBr₃ microplate showed long-term stability and good lifetime performance. Our findings provided a meaningful reference for the design of outstanding photoelectric devices.

Author Contributions: Conceptualization, X.W.; methodology, X.W.; software, X.W., F.Y., J.H., Y.Y.; validation, F.X.; formal analysis, X.W.; investigation, X.W.; resources, F.X., X.W., F.Y., J.H., Y.Y.; data curation, X.W.; writing—original draft preparation, X.W.; writing—review and editing, X.W. and F.X.; visualization, X.W.; supervision, F.X.; project administration, F.X.; funding acquisition, F.X. All authors have read and agreed to the published version of the manuscript.

Funding: This research was funded by the National Natural Science Foundation of China (no. 11575187) and the National Key Research and Development Program (no. 2016YFB0700205).

Institutional Review Board Statement: Not applicable.

Informed Consent Statement: Not applicable.

Data Availability Statement: Not applicable.

Conflicts of Interest: The authors declare no conflict of interest.

References

- Zhao, Y.; Qiu, Y.; Feng, J.; Zhao, J.; Chen, G.; Gao, H.; Zhao, Y.; Jiang, L.; Wu, Y. Chiral 2D-Perovskite Nanowires for Stokes Photodetectors. *J. Am. Chem. Soc.* **2021**, *143*, 8437–8445. [[CrossRef](#)] [[PubMed](#)]
- Lu, C.H.; Biesold-Mcgee, G.V.; Liu, Y.; Kang, Z.; Lin, Z. Doping and ion substitution in colloidal metal halide perovskite nanocrystals. *Chem. Soc. Rev.* **2020**, *49*, 4953–5007. [[CrossRef](#)] [[PubMed](#)]
- Swarnkar, A.; Marshall, A.R.; Sanehira, E.M.; Chernomordik, B.D.; Moore, D.T.; Christians, A.J.; Luther, J.M. Tamoghna Chakrabarti. Quantum dot-induced phase stabilization of a-CsPbI₃ perovskite for high-efficiency photovoltaics. *Science* **2016**, *354*, 92–96. [[CrossRef](#)] [[PubMed](#)]
- Shi, Z.; Li, Y.; Zhang, Y.; Chen, Y.; Li, X.; Wu, D.; Xu, T.; Shan, C.; Du, G. High-efficiency and air-stable perovskite quantum dots light-emitting diodes with an all-inorganic heterostructure. *Nano Lett.* **2017**, *17*, 313–321. [[CrossRef](#)] [[PubMed](#)]
- Li, X.; Bi, D.; Yi, C.; Décoppet, J.D.; Luo, J.; Zakeeruddin, S.M.; Hagfeldt, A.; Grätzel, M. A vacuum flash-assisted solution process for high-efficiency large-area perovskite solar cells. *Science* **2016**, *353*, 58–62. [[CrossRef](#)] [[PubMed](#)]
- Zhou, H.; Chen, Q.; Li, G.; Luo, S.; Song, T.B.; Duan, H.-S.; Hong, Z.; You, J.; Liu, Y.; Yang, Y. Interface engineering of highly efficient perovskite solar cells. *Science* **2014**, *345*, 542–546. [[CrossRef](#)]
- Liao, L.; Quan, K.; Bin, X.; Zeng, R.; Lin, T. Bandgap and Carrier Dynamic Controls in CsPbBr₃ Nanocrystals Encapsulated in Polydimethylsiloxane. *Crystals* **2021**, *11*, 1132. [[CrossRef](#)]
- Zhang, Q.; Yin, Y. All-Inorganic Metal Halide Perovskite Nanocrystals: Opportunities and Challenges. *ACS Cent. Sci.* **2018**, *4*, 668–679. [[CrossRef](#)]

9. Stranks, S.D.; Burlakov, V.M.; Leijtens, T.; Ball, J.M.; Goriely, A.; Snaith, H.J. Recombination Kinetics in Organic-Inorganic Perovskites: Excitons, Free Charge, and Subgap States. *Phys. Rev. Appl.* **2014**, *2*, 034007. [[CrossRef](#)]
10. Zhu, H.; Fu, Y.; Meng, F.; Wu, X.; Gong, Z.; Ding, Q.; Gustafsson, M.V.; Trinh, M.T.; Jin, S.; Zhu, X.Y. Lead halide perovskite nanowire lasers with low lasing thresholds and high quality factors. *Nat. Mater.* **2015**, *14*, 636–642. [[CrossRef](#)]
11. Stoumpos, C.C.; Malliakas, C.D.; Peters, J.A.; Liu, Z.; Sebastian, M.; Im, J.; Chasapis, T.C.; Wibowo, A.C.; Chung, D.Y.; Freeman, A.J.; et al. Crystal Growth of the Perovskite Semiconductor CsPbBr₃: A New Material for High-Energy Radiation Detection. *Cryst. Growth Des.* **2013**, *13*, 2722–2727. [[CrossRef](#)]
12. Yin, W.J.; Shi, T.; Yan, Y. Unusual defect physics in CH₃NH₃PbI₃ perovskite solar cell absorber. *Appl. Phys. Lett.* **2014**, *104*, 063903. [[CrossRef](#)]
13. Li, M.; Wei, Q.; Muduli, S.K.; Yantara, N.; Xu, Q.; Mathews, N.; Mhaisalkar, S.G.; Xing, G.; Sum, T.C. Enhanced Exciton and Photon Confinement in Ruddlesden–Popper Perovskite Microplatelets for Highly Stable Low-Threshold Polarized Lasing. *Adv. Mater.* **2018**, *30*, e1707235. [[CrossRef](#)] [[PubMed](#)]
14. Ling, Y.; Tian, Y.; Wang, X.; Wang, J.C.; Knox, J.M.; Perez-Orive, F.; Du, Y.; Tan, L.; Hanson, K.; Ma, B.; et al. Enhanced Optical and Electrical Properties of Polymer-Assisted All-Inorganic Perovskites for Light-Emitting Diodes. *Adv. Mater.* **2016**, *28*, 8983–8989. [[CrossRef](#)] [[PubMed](#)]
15. Han, Y.; Wen, R.; Zhang, F.; Shi, L.; Wang, W.; Ji, T.; Li, G.; Hao, Y.; Feng, L.; Cui, Y. Photodetector Based on CsPbBr₃/Cs₄PbBr₆ Composite Nanocrystals with High Detectivity. *Crystals* **2021**, *11*, 1287. [[CrossRef](#)]
16. Hodes, G.; Cahen, D. Perovskite cells roll forward. *Nat. Photonics* **2014**, *8*, 87–88. [[CrossRef](#)]
17. Noh, J.H.; Im, S.H.; Heo, J.H.; Mandal, T.N.; Seok, S.I. Chemical management for colorful, efficient, and stable inorganic-organic hybrid nanostructured solar cells. *Nano Lett.* **2013**, *13*, 1764–1769. [[CrossRef](#)]
18. Leguy, A.M.A.; Hu, Y.; Campoy-Quiles, M.; Alonso, M.I.; Weber, O.J.; Azarhoosh, P.; van Schilfgaarde, M.; Weller, M.T.; Bein, T.; Nelson, J.; et al. Reversible hydration of CH₃NH₃PbI₃ in films, single crystals, and solar cells. *Chem. Mater.* **2015**, *27*, 3397–3407. [[CrossRef](#)]
19. Akbulatov, A.F.; Luchkin, S.Y.; Frolova, L.A.; Dremova, N.N.; Gerasimov, K.L.; Zhidkov, I.S.; Anokhin, D.V.; Kurmaev, E.Z.; Stevenson, K.J.; Troshin, P.A. Probing the Intrinsic Thermal and Photochemical Stability of Hybrid and Inorganic Lead Halide Perovskites. *J. Phys. Chem. Lett.* **2017**, *8*, 1211–1218. [[CrossRef](#)]
20. Møller, C.H.R.K.N. Crystal Structure and Photoconductivity of Caesium Plumbohalides. *Nature* **1958**, *182*, 1436. [[CrossRef](#)]
21. Liang, J.; Zhu, G.; Wang, C.; Zhao, P.; Wang, Y.; Hu, Y.; Ma, L. Nano Energy An all-inorganic perovskite solar capacitor for efficient and stable spontaneous photocharging. *Nano Energy* **2018**, *52*, 239–245. [[CrossRef](#)]
22. Xue, M.; Zhou, H.; Ma, G.; Yang, L.; Song, Z.; Zhang, J.; Wang, H. Solar Energy Materials and Solar Cells Investigation of the stability for self-powered CsPbBr₃ perovskite photodetector with an all-inorganic structure. *Sol. Energy Mater. Sol. Cells* **2018**, *187*, 69–75. [[CrossRef](#)]
23. Hossain, M.T.; Das, M.; Ghosh, J.; Ghosh, S.; Giri, P.K. Understanding the interfacial charge transfer in the CVD grown Bi₂O₂Se/CsPbBr₃ nanocrystal heterostructure and its exploitation in superior photodetection: Experiment vs. theory. *Nanoscale* **2021**, *13*, 14945–14959. [[CrossRef](#)]
24. Swarnkar, A.; Chulliyil, R.; Ravi, V.K.; Irfanullah, M.; Chowdhury, A.; Nag, A. Colloidal CsPbBr₃ Perovskite Nanocrystals: Luminescence beyond Traditional Quantum Dots. *Angew. Chem.* **2015**, *127*, 15644–15648. [[CrossRef](#)]
25. Ghosh, J.; Hossain, M.; Giri, P.K. Origin and tunability of dual color emission in highly stable Mn doped CsPbCl₃ nanocrystals grown by a solid-state process. *J. Colloid Interface Sci.* **2020**, *564*, 357–370. [[CrossRef](#)] [[PubMed](#)]
26. Ghosh, J.; Mawlong, L.P.L.; Manasa, B.G.; Pattison, A.J.; Theis, W.; Chakraborty, S.; Giri, P.K. Solid-state synthesis of stable and color tunable cesium lead halide perovskite nanocrystals and the mechanism of high-performance photodetection in a monolayer MoS₂/CsPbBr₃ vertical heterojunction. *J. Mater. Chem. C* **2020**, *8*, 8917–8934. [[CrossRef](#)]
27. Tang, B.; Dong, H.; Sun, L.; Zheng, W.; Wang, Q.; Sun, F.; Jiang, X.; Pan, A.; Zhang, L. Single-Mode Lasers Based on Cesium Lead Halide Perovskite Submicron Spheres. *ACS Nano* **2017**, *11*, 10681–10688. [[CrossRef](#)] [[PubMed](#)]
28. Gao, Y.; Li, X.; Liu, W.; Xing, X.; Long, H.; Wang, K.; Wang, B.; Lu, P. Highly Tunable Enhancement and Switching of Nonlinear Emission from All-Inorganic Lead Halide Perovskites via Electric Field. *Nano Lett.* **2021**, *21*, 10230–10237. [[CrossRef](#)]
29. Zhang, X.; Chen, S.; Wang, X.; Pan, A. Controlled Synthesis and Photonics Applications of Metal Halide Perovskite Nanowires. *Small Methods* **2019**, *3*, 1–17. [[CrossRef](#)]
30. Geng, D.; Wu, B.; Guo, Y.; Luo, B.; Xue, Y.; Chen, J.; Yu, G.; Liu, Y. Fractal etching of graphene. *J. Am. Chem. Soc.* **2013**, *135*, 6431–6434. [[CrossRef](#)]
31. Wang, S.; Rong, Y.; Fan, Y.; Pacios, M.; Bhaskaran, H.; He, K.; Warner, J.H. Shape evolution of monolayer MoS₂ crystals grown by chemical vapor deposition. *Chem. Mater.* **2014**, *26*, 6371–6379. [[CrossRef](#)]
32. Wang, X.; He, J.; Li, J.; Lu, G.; Dong, F.; Majima, T.; Zhu, M. Immobilizing perovskite CsPbBr₃ nanocrystals on Black phosphorus nanosheets for boosting charge separation and photocatalytic CO₂ reduction. *Appl. Catal. B Environ.* **2020**, *277*, 119230. [[CrossRef](#)]
33. Wang, Y.; Guan, X.; Li, D.; Cheng, H.C.; Duan, X.; Lin, Z.; Duan, X. Chemical vapor deposition growth of single-crystalline cesium lead halide microplatelets and heterostructures for optoelectronic applications. *Nano Res.* **2017**, *10*, 1223–1233. [[CrossRef](#)]
34. Cao, Y.; Luo, X.; Han, S.; Yuan, C.; Yang, Y.; Li, Q.; Yu, T.; Ye, S. Influences of carrier gas flow rate on the morphologies of MoS₂ flakes. *Chem. Phys. Lett.* **2015**, *631–632*, 30–33. [[CrossRef](#)]

35. Cha, J.H.; Han, J.H.; Yin, W.; Park, C.; Park, Y.; Ahn, T.K.; Cho, J.H.; Jung, D.Y. Photoresponse of CsPbBr₃ and Cs₄PbBr₆ Perovskite Single Crystals. *J. Phys. Chem. Lett.* **2017**, *8*, 565–570. [[CrossRef](#)]
36. He, Y.; Su, R.; Huang, Y.; Zhou, Y.; Zhao, Q.; Khurgin, J.B. High-Order Shift Current Induced Terahertz Emission from Inorganic Cesium Bromine Lead Perovskite Engendered by Two-Photon Absorption. *Adv. Funct. Mater.* **2019**, *29*, 1904694. [[CrossRef](#)]
37. Lian, Z.; Yan, Q.; Gao, T.; Ding, J.; Lv, Q.; Ning, C.; Li, Q.; Sun, J.L. Perovskite CH₃NH₃PbI₃(Cl) Single Crystals: Rapid Solution Growth, Unparalleled Crystalline Quality, and Low Trap Density toward 10⁸ cm⁻³. *J. Am. Chem. Soc.* **2016**, *138*, 9409–9412. [[CrossRef](#)]
38. Zhang, M.; Zheng, Z.; Fu, Q.; Chen, Z.; He, J.; Zhang, S.; Chen, C.; Luo, W. Synthesis and single crystal growth of perovskite semiconductor CsPbBr₃. *J. Cryst. Growth* **2018**, *484*, 37–42. [[CrossRef](#)]